Article

Framework for Geometric Information Extraction and Digital Modeling from LiDAR Data of Road Scenarios

Yuchen Wang [1], Weicheng Wang [2], Jinzhou Liu [1], Tianheng Chen [1], Shuyi Wang [1], Bin Yu [1,*] and Xiaochun Qin [3]

1   School of Transportation, Southeast University, #2 Southeast University Road, Nanjing 211189, China
2   China Design Group Co., Ltd., Nanjing 210014, China
3   School of Civil Engineering, Beijing Jiaotong University, No.3 Shangyuancun, Beijing 100044, China
*   Correspondence: yb@seu.edu.cn

Abstract: Road geometric information and a digital model based on light detection and ranging (LiDAR) can perform accurate geometric inventories and three-dimensional (3D) descriptions for as-built roads and infrastructures. However, unorganized point clouds and complex road scenarios would reduce the accuracy of geometric information extraction and digital modeling. There is a standardization need for information extraction and 3D model construction that integrates point cloud processing and digital modeling. This paper develops a framework from semantic segmentation to geometric information extraction and digital modeling based on LiDAR data. A semantic segmentation network is improved for the purpose of dividing the road surface and infrastructure. The road boundary and centerline are extracted by the alpha-shape and Voronoi diagram methods based on the semantic segmentation results. The road geometric information is obtained by a coordinate transformation matrix and the least square method. Subsequently, adaptive road components are constructed using Revit software. Thereafter, the road route, road entity model, and various infrastructure components are generated by the extracted geometric information through Dynamo and Revit software. Finally, a detailed digital model of the road scenario is developed. The Toronto-3D and Semantic3D datasets are utilized for analysis through training and testing. The overall accuracy (OA) of the proposed net for the two datasets is 95.3 and 95.0%, whereas the IoU of segmented road surfaces is 95.7 and 97.9%. This indicates that the proposed net could accomplish superior performance for semantic segmentation of point clouds. The mean absolute errors between the extracted and manually measured geometric information are marginal. This demonstrates the effectiveness and accuracy of the proposed extraction methods. Thus, the proposed framework could provide a reference for accurate extraction and modeling from LiDAR data.

Keywords: LiDAR data; road engineering; point cloud processing; semantic segmentation; digital modeling

1. Introduction

As-built roads have received much more attention from road administration agencies after years of operation, which requires extensive field measurements to update the corresponding information based on a data model or technology, such as Building Information Modeling (BIM) [1]. Geometric and semantic information on as-built roads and infrastructures is essential to cover a wide range of topics, including asset management and road safety inspection [2,3]. Advanced information and sensing technologies have been increasingly applied in road maintenance and management with the increase in the number of as-built roads and higher requirements of construction management [4]. Light detection and ranging (LiDAR) is a reliable and efficient technology widely used in road geometry measurements, obstacle detection, and landscape modeling [5,6]. This technology could provide high quality point clouds [7]. However, these point cloud data do not contain semantic and geomatic information. Moreover, road scenarios are complex and

contain multiple types of objects. This decreases the precision of semantic segmentation and geometric information extraction. In particular, the data gathered through LiDAR technology is a collection of unorganized, irregularly sampled, and unstructured point clouds [8], which increases the difficulty of converting the point clouds into semantic-rich models of as-built roads and different categories of infrastructures. Thus, it is important to establish an accurate and effective framework that takes, as input, point clouds from LiDAR systems and outputs a digital model to interlink 3D point clouds regarding the geometric and semantic information of as-built roads and surrounding infrastructures.

Within this context, the road surface is an important road design structure, representing the geometric information of the road. Roadside infrastructure is essential for traffic-related applications and safe operation. Hence, segmentation of road surfaces and infrastructures is the first step for generating detailed geometric elements. The studies related to road surface segmentation from point clouds have focused on three categories: structure-driven, feature–driven, and model-driven methods [9–11]. Structure-driven methods rely on the detection of curbs to define the road boundary and the subsequent extraction of the road surface [12]. These methods have been developed for curb detection using different data sources, including the scan lines, density and elevation of 3D point clouds [13,14], and two-dimensional geo-referenced feature (2D GRF) images generated by the projection of the 3D point clouds [15,16]. Although good results were attained from these works, the segmentation of the road surface is not robust when it is not delimited by curbs, which is the case for most non-urban roads. Feature–driven methods are performed based on previous knowledge of geometric and contextual features, such as roughness and the height of road surfaces [17,18]. However, these approaches require a substantial number of fixed thresholds, which need to be defined or tested by the user. Model-driven methods primarily refer to the semantic segmentation of road surfaces by deep neural networks. These can be largely divided into three categories [19]: projection-based [20], discretization-based [21–23], and point-based methods [24]. The first two methods convert the point clouds into other regular representations, such as 2D images and 3D grids. This causes information loss and incurs computation expense for the projection back to the original dimension [25]. Unlike the above methods, point-based methods (e.g., PointNet and PointNet++) directly work on the point clouds. For large-scale point clouds containing hundreds of objects, the widely employed farthest point sampling cannot efficiently and rapidly process a large number of points. Thus, the pioneering RandLA-Net [26] was proposed as a potential approach developed on the principles of random sampling (RS). However, it fails to capture wider context information for different and similar features owing to the removal of key features caused by the RS method [27].

In addition, numerous studies have examined the geometric information extraction methods based on point clouds and other data sources, such as the Geographic Information Systems (GIS) database [28,29], optical images [30], or vehicle trajectory obtained by Global Positioning System (GPS) [31] or Inertial Measurement Units (IMU) [32]. According to the above analysis, the accuracy of geometric element extraction is severely affected by the captured data sources. However, the accurate extraction of geometric information using optical images is challenging because of low illumination and inclement weather. Furthermore, certain extraction methods based on trajectory data may not satisfy the requirements of a stationary system. In addition, the integrity and accuracy of the obtained trajectory are limited in complex road scenarios owing to the movement of vehicles with larger fluctuations and away from the centerline of the road.

Finally, and in the context of digital modeling using 3D point clouds, Justo et al. proposed a semi-automatic modeling approach for traffic signs, guardrails, and other road elements via BIM [33]. In addition, they modeled the alignment and centerline of each road lane on a highway through BIM and GIS [34]. Tang et al. developed a framework for integrating road design and pavement analysis relying on the capabilities of Dynamo [35]. However, these approaches only focused on separate objects, rather than considering the integration of the road and other infrastructures in a real-world space or their relationship.

The objective of this paper is to present a framework that accepts raw point clouds from various LiDAR systems as input, and outputs an integrated digital model that represents the geometric and semantic information of the road and other infrastructure. The main contributions of this study are as follows:

(1)　An improved semantic segmentation network that accurately and efficiently divides the road surface and other infrastructure.

(2)　A series of geometric information extraction methods that can be used to obtain the road boundary and centerline, and to calculate the geometric elements of roads. These can be applied to the segmented point clouds that contain 3D coordinates and RGB information. Note that the extraction methods do not aim to be the contribution. However, these are essential for the entire workflow and would be validated if the mean absolute errors between the extracted and manually measured geometric information were marginal.

(3)　A digital modeling process that constructs a road entity model and various infrastructure components to realize a geometric representation.

2. Materials and Methods

This section is divided into four subsections. The first analyzes the point clouds obtained by different LiDAR systems. After a brief overview of the methods, a detailed description of the main processing steps is provided. In particular, point cloud semantic segmentation and the extraction of road geometric information are described. The digital modeling of road scenarios is described in detail.

2.1. Point Clouds Obtained by Different LiDAR Systems

Considering the platform type employed to install the system, there are three types of arrangements of laser scanner systems: terrestrial laser scanner (TLS), aerial laser scanner (ALS), and mobile laser scanner (MLS) [36]. A TLS is a stationary system consisting of a LiDAR device mounted on a tripod or other type of stand. It is capable of obtaining high-resolution scans of complex scenarios. The point clouds captured by TLS contain 3D coordinates, RGB information, and intensity [37]. With regard to ALS, the laser scanner is installed on an aircraft (typically an airplane) based on GNSS receivers and IMU. The ALS can record the 3D coordinates and intensity of each echo, and colorize point clouds through digital photographs captured by a calibrated camera [38]. Finally, the MLS is integrated with multiple on-board sensors comprising a GNSS system, an IMU, and a DMI. However, in certain cases, the data processing methods used in TLS or ALS cannot be directly applied to MLS. This is owing to differences in the manner of data acquisition, mainly the geometry of the scanning and point density [39]. Therefore, our study is implemented based on per-point features (e.g., 3D coordinates and RGB information). It focuses on the content of acquired data rather than the LiDAR systems, thereby ensuring the universality of the proposed methods.

2.2. Methods Overview

The methodology proposed in this paper is divided into three steps (see Figure 1): (1) semantic segmentation, (2) geometric information extraction, and (3) BIM technology for digital modeling. The raw point cloud data do not possess semantic and geomatic information, and road scenarios are complex and contain multiple types of objects. Therefore, we first segment the road surfaces and infrastructures in the process of semantic segmentation. More specifically, the improved semantic segmentation network is proposed in Step 1. Based on a fundamental foundation of SCF-Net, the aggregated attention pooling module is improved to describe the difference and similarity of local features. Then, 3D coordinates and radial distributions are gathered to enrich global contextual features and preserve the complex geometric structure of point clouds. The road surfaces and other categories of infrastructure are segmented by this procedure. In Step 2, the road boundary and centerline are extracted by the alpha-shape method and Voronoi diagram (or Thiessen-Polygons)

method based on the segmented road surfaces. Subsequently, the geometric information is obtained from the 3D coordinates of the road boundary and centerline. Finally, the road centerline and geometric information is imported to generate a road route through Dynamo. Adaptive road components are developed and placed to form a complete road entity model based on the generated road route. Given the segmented infrastructures in Step 1, the locations of infrastructures are determined and fitted. The road entity model and various infrastructure components, such as guardrails and buildings, are constructed and arranged using Revit software. Thereby, the details of vegetation and other elements are manually adjusted based on the imported point clouds, and the digital road scenario is established.
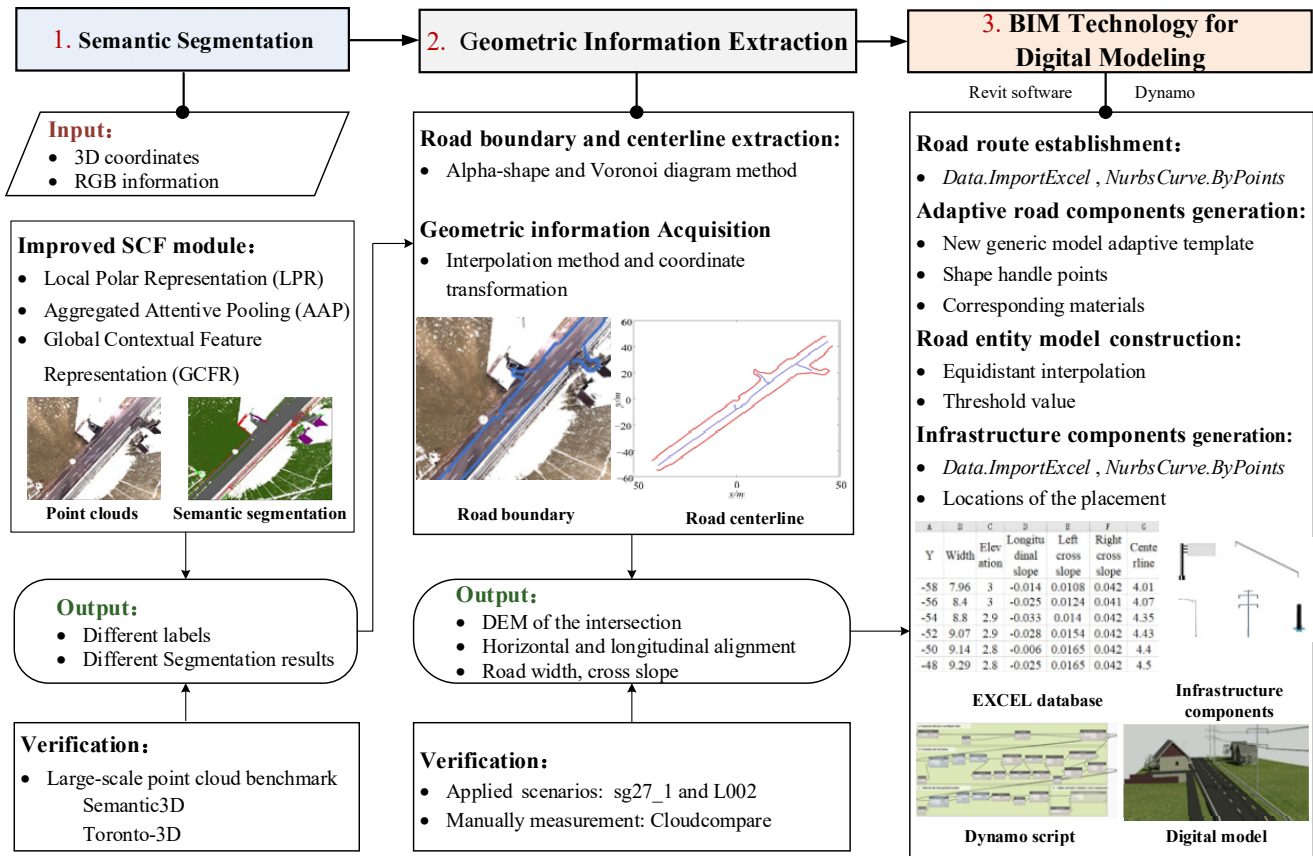

Figure 1. Workflow of the methods.

2.3. Semantic Segmentation of Point Clouds

The large scale of point clouds incurs high computational and memory costs owing to the wide space of road scenarios, including the road surface, vegetation, infrastructure, buildings, and other categories of objects. Consequently, an efficient and lightweight deep neural network needs to be applied to directly infer per-point semantics for large-scale point clouds, and thereby realize multi-object recognition and segmentation. Large-scale point cloud semantic segmentation networks have been proposed, such as RandLA-Net and SCF-Net. SCF-Net can achieve high efficiency using the RS method and generate point-wise representations of spatial information. However, the RS method would unintentionally discard key features [40]. It is worth mentioning that the collected point clouds may include noise and unclear objects at a distance from the sensor. These affect the accuracy of semantic segmentation. It is difficult to reflect the different and similar features of local point clouds because the point clouds would be inadequate and sparse during the sampling process. To address these subproblems, we propose an improved SCF-Net for raw point clouds to aggregate the different and similar local contextual features, and optimize global contextual features. This would enhance the capability to learn effective spatial contextual features

from large-scale point clouds. We introduce the proposed module in detail in this section and describe the architecture of the improved SCF-Net in the following subsection.

2.3.1. Improved SCF Module

We improved the SCF module to extract local and global contextual features of point clouds. It consists of three blocks: local polar representation (LPR), aggregated attentive pooling (AAP), and global contextual feature representation (GCFR). We introduce the architecture of the improved SCF-Net. It has an encoder-decoder with the SCF module.

It is observed that the improved SCF module is applied to aggregate the local maximum and mean features of neighboring points to extract more local contextual features and reduce the redundant information in an AAP neural unit. In a GCFR neural unit, 3D coordinates and radial distributions are utilized as global contextual features to represent the distribution of point clouds in 3D space (see Figure 2).

1. Local Polar Representation

It is notable that, in certain real scenarios, segmentation performance is hindered by different orientations of the same category of objects. For example, vehicles parked in different orientations on the roadside may be misconstrued as roadside infrastructures [41]. We apply the method proposed by Fan [27] to reduce the influence of object orientation on the geometric features. Evidently, the LPR unit is established in the polar coordinate system that is invariant along the *z*-axis. Furthermore, the local context of point clouds is converted from Cartesian coordinates to polar coordinates.

First, a point and its *k*-nearest neighboring points are obtained in the polar coordinate system. Thereafter, the geometric distance and original relative angles are calculated. Then, the center-of-mass of the neighboring points is determined, and the local direction is defined from a point to its center-of-mass. In addition, the updated relative angles are obtained by the original relative angles and relative angles. Finally, the updated relative angles and geometric distance are combined as the geometric patterns.

2. Aggregated Attentive Pooling

The AAP unit is developed by integrating the local and neighboring point features to measure geometric details among large-scale point clouds and learn local contextual features. In an AAP unit, the geometric distance, point features, and geometric patterns are obtained as inputs. This proposed unit entails the following steps:

Computing the feature distance: The L_1 norm and mean function are used to calculate the feature distance between the input feature vectors of the *i*-th point and its *k*-th neighboring point [27]. This can be expressed as

$$dis_{if}^k = \text{mean}(|v(i)| - |v(k)|) \tag{1}$$

where dis_{if}^k denotes the feature distance, $|\ \ |$ is the L_1 norm, and mean $(\cdot)$ is the mean function. $v(i)$ and $v(k)$ denote feature vectors of the *i*-th point and its *k*-th neighboring point, respectively.

Determining the attentive pooling weights: The geometric distance and feature distance can measure the correlation among points in the world and feature space. The smaller the distance, the higher their relevance. Meanwhile, the weights lie in [0,1]. Hence, the geometric distance and feature distance are transformed through a negative exponential, and combined to define the aggregated distance dis_i^k:

$$dis_i^k = \text{concat}(\exp\left(-dis_{ig}^k\right), \exp\left(-dis_{if}^k\right)) \tag{2}$$

where dis_{ig}^k and dis_{if}^k are the geometric distance and feature distance, respectively.

Given the aggregated distance dis_i^k, we combine point features f_i^κ to obtain the set of local features dis_i^l through a concatenation operator. Then, we use a shared MLP followed by Softmax to learn the attentive pooling weight w_i^k for dis_i^l.
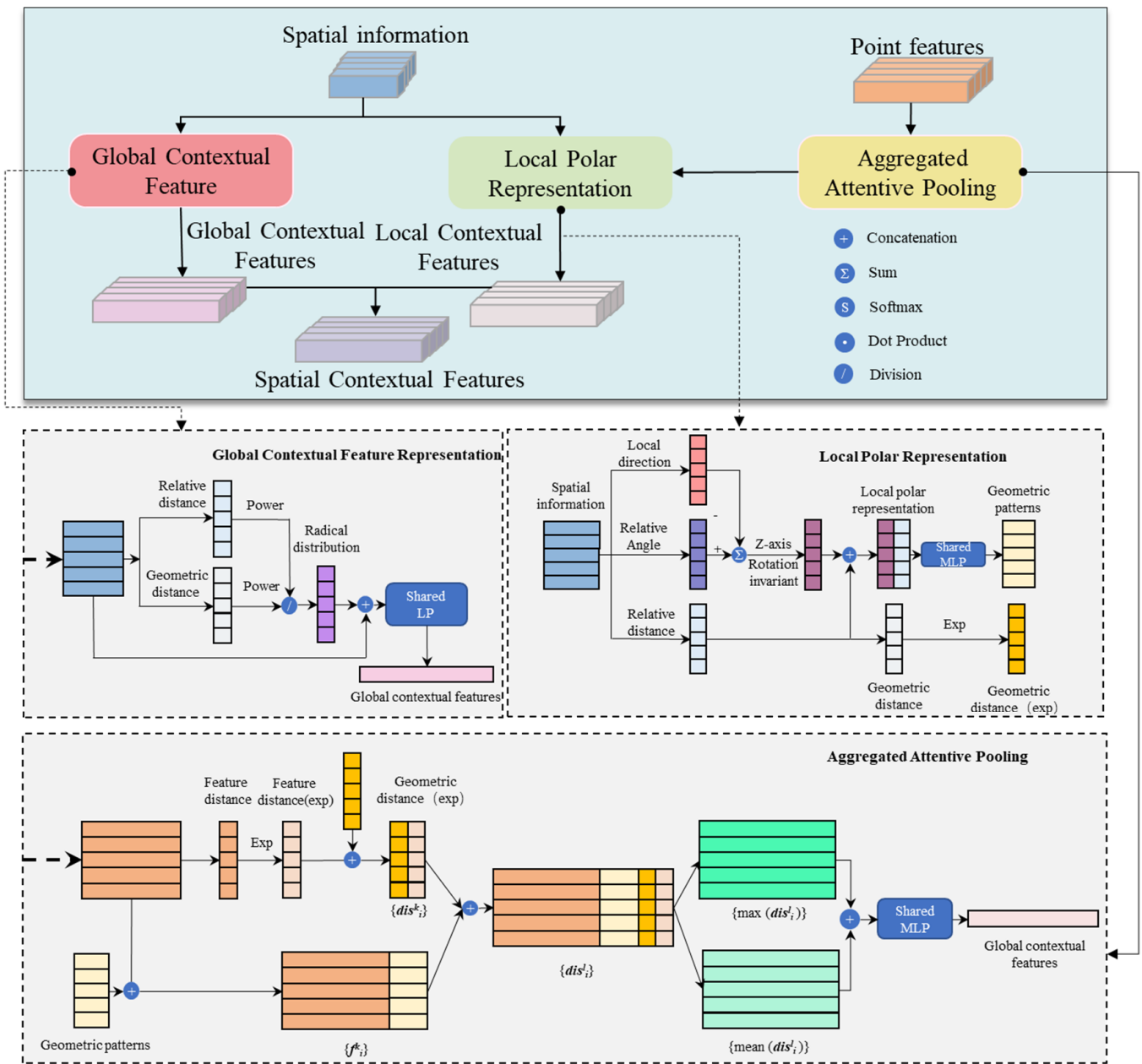
Figure 2. Improved SCF module.

Calculating local contextual features: First, the maximum features $\max_k\left(\boldsymbol{dis}_i^l\right)$ from the neighboring point features are directly collected to show the local distinctness. Then, the neighboring point mean features $\underset{k,w_i^k}{\text{mean}}\left(\boldsymbol{dis}_i^l\right)$ are defined by re-weighting the neighboring point features with w_i^k to closely gather similar local context. Finally, we combine the two types of features to precisely capture and learn local contextual features $\boldsymbol{f}_{iL}$ by utilizing the neighboring point features.

$$f_{iL} = \text{concat}\left(\max_k\left(\boldsymbol{dis}_i^l\right), \underset{k,w_i^k}{\text{mean}}\left(\boldsymbol{dis}_i^l\right)\right) \tag{3}$$

3. Global Contextual Feature Representation

Given the local contextual features, the context among the neighboring points is not sufficiently discriminative for semantic segmentation. The global contextual features can be used to learn complex geometric structures and enrich the global context from 3D points. These two contextual features can be concatenated to obtain spatial contextual features.

It is noted that different objects of the same category may have certain differences in global spatial features owing to different locations and scenarios. Furthermore, their geometric architectures are generally similar. The radial distribution is utilized as the supplement of global contextual features. It reflects the distribution of point clouds in the world space [42], which is defined as follows:

$$r_i = \frac{\rho_l^i}{\rho_g^i} = \frac{N_k^i}{N_g^i} \cdot \left(\frac{R_l^i}{R_g^i} \right)^3 \tag{4}$$

where r_i is the radial distribution; ρ_l^i and ρ_g^i are the densities of the neighboring points and global point clouds, respectively; N_k^i and N_g^i are the numbers of neighboring points and global points, respectively. R_l^i and R_g^i are the local and global radii, respectively.

The radial distribution could combine the local and global information distribution and is irrelevant to the per-point distribution. Evidently, the radial distribution is insensitive to marginal geometric deformations, thereby reserving the global information and geometric structures. In addition, the 3D coordinates of a point p_i are used to represent the location of local neighboring points. Therefore, 3D coordinates are combined with radial distribution as global contextual features. This is defined as follows:

$$f_{ig} = \text{concat}(\text{MLP}(x_i, y_i, z_i), r_i) \tag{5}$$

2.3.2. Architecture of Improved SCF-Net

In this subsection, the improved SCF module is embedded in a standard encoder-decoder architecture to yield the improved SCF-Net. It consists of fully connected layers, and encoder and decoder layers (see Figure 3). A fully connected layer is first used to extract the per-point features. In addition, five encoders are used to reduce the point cloud size and increase the feature dimension. More specially, the number of point clouds is downsampled through the RS method. The improved module can learn effective spatial contextual features to prevent loss of valid information caused by the RS method. Then, decoder layers are used after the above encoder layers. The encoded feature dimension is then upsampled through a nearest-neighbor interpolation. The upsampled features are concatenated with the intermediate features produced by the encoder layers through skip connections. Thereafter, a shared MLP is used to concatenate the features before and after sampling. Finally, three fully connected layers and a dropout layer are applied to predict the semantic labels. Furthermore, the cross-entropy loss is used for training.

2.4. Process of Road Geometric Information Extraction

The geometric information, including the horizontal alignment, vertical alignment, and cross-section of the road (particularly the elevation of intersections), needs to be obtained for the as-built survey or traffic safety analysis. Evidently, the digital elevation model (DEM) of the intersection is established to provide the basis for calculating the sight distance, analyzing traffic conflicts, and reconstructing intersections. Therefore, we propose a series of geometric information extraction methods for segmented point clouds from various LiDAR systems. To guarantee the reliability and versatility of the methods, we use 3D coordinates and RGB information as per-point features, lacking timestamps and echo times. Accordingly, certain methods based on scan lines are unsuitable for geometric information and track extraction [43,44].
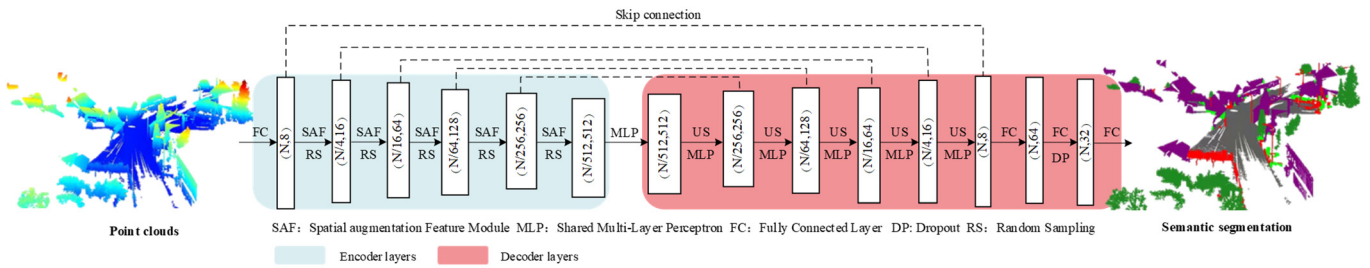
Figure 3. Architecture of improved SCF-Net.

Given the segmented road surface, the alpha-shape method is first used to preserve polygonal details of the finite points for boundary reconstruction [45]. The parameter α identifies the radius of the rolling circles around the road, which controls the precision of the boundary [46]. Thereafter, the centerline can be extracted by the Voronoi diagram (or Thiessen-Polygons) method depending on the calculated road boundary points. Moreover, extraneous lines are removed by several iterations and a minimum threshold [47,48]. Finally, the geometric information calculations based on the road boundary and centerline entail the following steps:

DEM of the intersection: Owing to the different densities of the captured road surface points, a uniformly distributed point set is first generated to calculate the elevation of the intersection. In particular, the range of the uniformly distributed point set is generated from x_{min} to x_{max} and from y_{min} to y_{max}. This forms a series of points with ε intervals. Thus, the number of the point set is $\left\lfloor \frac{y_{max} - y_{min}}{\varepsilon} \right\rfloor \times \left\lfloor \frac{x_{max} - x_{min}}{\varepsilon} \right\rfloor$ ('$\lfloor \ \rfloor$' implies floor function). Moreover, the inShape function in MATLAB is used to assess and reserve the road surface points within the extracted boundary of the intersection. The elevation of each point in the point set is determined by the interpolation method based on the elevation and distance of two adjacent road surface points. This can be expressed as

$$Z_i = \frac{d_i^b}{d_i^a + d_i^b} \cdot z_i^a + \frac{d_i^a}{d_i^a + d_i^b} \cdot z_i^b \qquad (6)$$

where Z_i denotes the elevation of the i-th point in the point set; z_i^a, z_i^b are the elevations of the two adjacent road surface points nearest to the i-th point; and d_i^a, d_i^b are the distances between the two adjacent road surface points and the i-th point.

Thus, the DEM of the intersection is established by integrating the elevation of the point set and the existing road surface points. Similarly, the DEM of the road can be constructed on the surface points within the road boundary.

Horizontal information: To decrease the difficulty of geometric information calculations, the curved road is transformed into a straight line by applying the coordinate transformation matrix of Equation (7). The original surface points are converted into transformed points based on the coordinates of the road centerline. Thus, the vertical and forward directions of the road are determined as the OX and OY directions, respectively. The horizontal alignment is generated by the transformed centerline.

$$\begin{bmatrix} X \\ Y \\ Z \end{bmatrix} = \begin{bmatrix} \cos(\theta) & -\sin(\theta) & 0 \\ \sin(\theta) & \cos(\theta) & 0 \\ 0 & 0 & 1 \end{bmatrix} \left(\begin{bmatrix} x \\ y \\ z \end{bmatrix} - \begin{bmatrix} x_0 \\ y_0 \\ z_0 \end{bmatrix} \right) + \begin{bmatrix} x_0 \\ y_0 \\ z_o \end{bmatrix}, \theta = \left(\frac{\pi}{2} - \phi \right) \qquad (7)$$

where X, Y, Z denote the 3D coordinates of the transformed point; θ is the transformation angle; ϕ is the grade of the road centerline; x, y, z are the 3D coordinates of the original surface points; and x_0, y_0, z_0 are the origin coordinates of the road centerline.

Vertical information: The elevation of the centerline is utilized to calculate the longitudinal slope of the road. Moreover, the relative elevation difference and horizontal

distance of the centerline are obtained. The quotient of the two values is computed as the longitudinal slope, which can be express as:

$$i_j = \frac{H_{j+1} - H_j}{W_{j+1,j}} = \frac{H_{j+1} - H_j}{\sqrt{\left(X_{j+1} - X_j\right)^2 + \left(Y_{j+1} - Y_j\right)^2}} \tag{8}$$

where H_j, H_{j+1}; X_j, X_{j+1}; and Y_j, Y_{j+1} denote the elevations, X-coordinates, and Y-coordinates, respectively, of the j-th and $j + 1$-th points of the centerline.

Cross-section information: First, the cross-sectional profile is represented in a vertical plane. It is computed as being perpendicular to the plane defined by the forward directions of the road. Thereafter, the identified cross-sectional profile is divided into left and right sides based on the centerline. The road width is calculated as the difference between the left and right sides. The least square method is then used to fit the cross-sectional profile on both sides, reducing the errors caused by the different densities of road surface points. Meanwhile, the errors between the fitting curves and the points of the profile are calculated. The slope of the fitting equation when the error is minimum is the cross slope.

2.5. BIM Technology for Digital Modeling

Based on the semantic segmentation of point clouds and the extraction of road geometric information, this study combines road 3D point clouds with BIM technology. In particular, the road entity and infrastructure modeling is established based on Dynamo and Revit. Dynamo is a visual programming software for geometric shapes, Revit diagram elements, and data interaction. The process of completing the parametric design of the road scenario entails the following steps.

To ensure that the work is feasible and effective in Dynamo, many nodes such as *Code Block*, *NurbsCurve.ByPoints*, and *Data.ImportExcel* are connected for editing. The process of digital modeling entails the following steps:

Setting the coordinate system: The point cloud of the road scenario is imported in Autodesk Recap and converted into rcp format. It can be inserted in Revit software to complement information for modeling. The point cloud and Revit file are set in the same coordinate system to ensure consistency with the position and orientation.

Generation of road route: Given the extracted road centerline and geometric information, the Excel database relevant to the 3D information of each stack is established. Thereafter, *Data.ImportExcel* is used to import the coordinate and geometric information (stack number, horizontal and vertical coordinates, elevation) from the Excel database. Finally, the imported coordinate data is fitted to generate the road route using *NurbsCurve.ByPoints*.

Setting adaptive road components: Considering the flexibility of an adaptive component in generative applications, we construct adaptive road components to adapt the actual road alignment. This process of generating an adaptive road component used by Revit software entails the following steps (see Figure 4).

First, a new generic model adaptive template is developed. Thereafter, the shape handle points are set and adjusted at the origin, midpoint, and destination of the adaptive component based on the direction of the road route, to ensure consistency with the design.

Additionally, another generic model adaptive template is created. In the template file, a cross-section is established. Thereby, a new shape handle point is generated and adjusted at the origin of the cross-section.

Finally, the origin of the cross-section is placed and loaded at the midpoint of the road route, generating the adaptive road component. The established adaptive road components associated with materials can be offered in the road entity model through Dynamo.
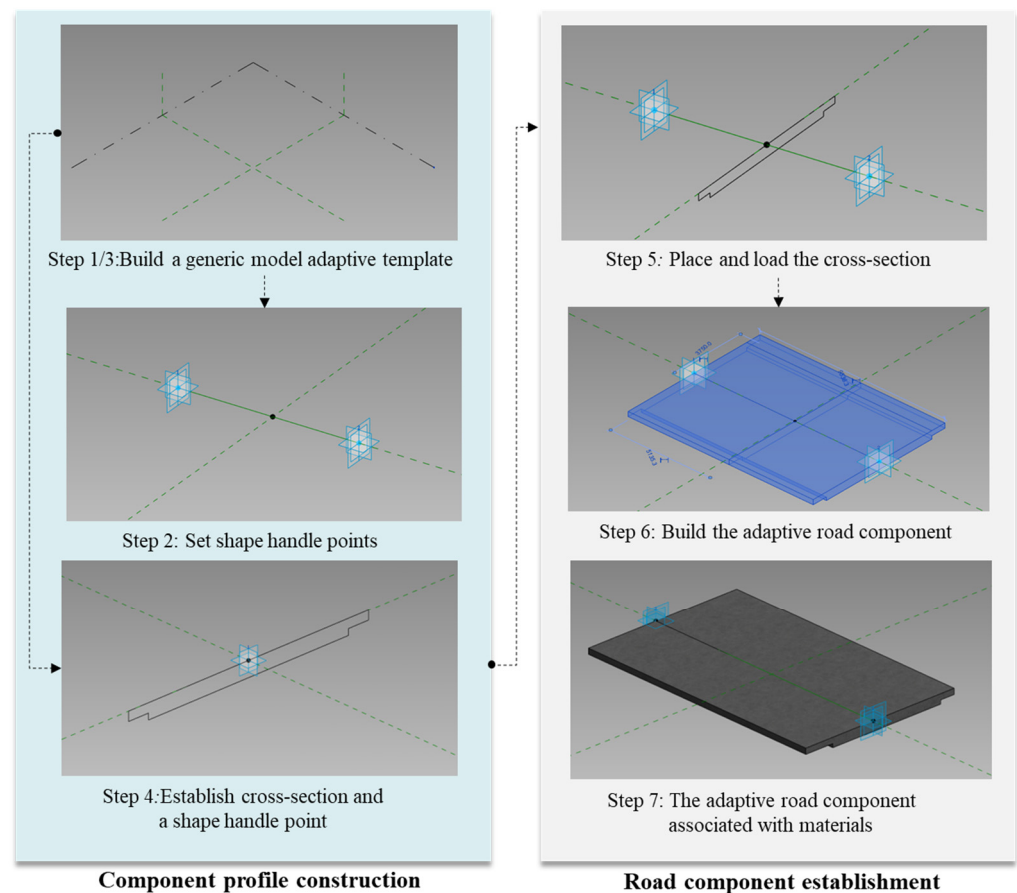
Figure 4. Setting of adaptive road components.

Establishment of the road entity model: First, a series of discrete coordinate data are obtained from the generated road route by equidistant interpolation. In addition, the deviation from each interpolation point to the road route is calculated in the *XOY* plane. The interpolation point is removed depending on the threshold value. Specifically, the processed interpolation points are allocated relying on the road alignment. When the road alignment is straight, two interpolation points are grouped as the origin and destination at the centerline of the adaptive road component. When the road alignment is a circular curve, three interpolation points are grouped as the origin, midpoint, and destination at the centerline of the adaptive road component. The cross-section is then adjusted to satisfy the requirements of widening and superelevation. For the transition curve, apart from setting the three interpolation points, additional shape handle points should be arranged at the origin, midpoint, and destination of the inner and outer roads. Accordingly, the designed adaptive components are placed among the group of interpolation points to form a complete road entity model using Dynamo.

Constructing the infrastructure components: Different categories of infrastructure components are constructed based on the semantic segmentation results. The data of the infrastructure boundary are imported through *Data.ImportExcel* first. The data is thereafter fitted to form boundary curves by *NurbsCurve.ByPoints*. Subsequently, the locations of placements are determined on the fitted boundary curves to construct different infrastructure. Finally, the infrastructure components are manually placed and constructed through Revit software.

Construction of 3D road scenario: Detailed designs are carried out for the road entity model and infrastructure components through Dynamo and Revit software. Evidently, the details of the surrounding environment are manually adjusted based on the imported point clouds. In addition, the road infrastructure assets and model information exchange and

sharing can be completed based on BIM technology by adding the records regarding name, age, and maintenance.

3. Results

3.1. Datasets and Implementation Detail

In this section, we train and evaluate the improved SCF-Net on two typical large-scale point cloud benchmarks: Toronto-3D [49] and Semantic3D [50]. The following includes a description of the datasets and the detailed implementation. Toronto-3D is a dataset related to urban roadways captured by the MLS system. It consists of four sections. Each point cloud owns the attributes of 3D coordinates, RGB information, intensity, GPS time, and scan angle rank. Semantic3D is related to urban and rural scenarios including streets, intersections, and rural roads. The TLS system is used for recording these scenarios. The raw 3D points are represented by 3D coordinates, RGB information, and intensity in the experiments.

Owing to the different acquired platform type, the attributes of each captured point cloud are dissimilar. Meanwhile, the manner of data acquisition affects the geometry of the scanning and point density. Therefore, our study uses two datasets from different LiDAR systems and focuses on the common attributes of acquired data to ensure the application of the proposed net. Because the intensity is significantly affected by the environment and illumination, we use 3D coordinates and RGB information of points for training and testing.

The experiments are implemented in Tensorflow on a server with NVDIA GTX-1080 TI GPU and CUDA 11.5. We use the Adam optimizer with default parameters. For example, the initial learning rate and batch size are set as 0.01 and 5, respectively. The network is trained for 100 epochs with a dropout ratio of 0.5. The number of neighbors is set to 16 ($k = 16$).

3.2. Semantic Segmentation on Benchmarks

We compare the proposed net with other state-of-the-art methods. We use the mean IoU (mIoU) and overall accuracy (OA) as standard metrics to evaluate the semantic segmentation of the proposed net on the Toronto-3D and Semantic3D datasets.

3.2.1. Evaluation on Toronto-3D

We select L002 as a test set for its smaller size and balanced number of points of each label. The mIoU and OA of the total eight categories are compared in Table 1. The visual comparison between point clouds and semantic segmentations is shown in Figure 5.
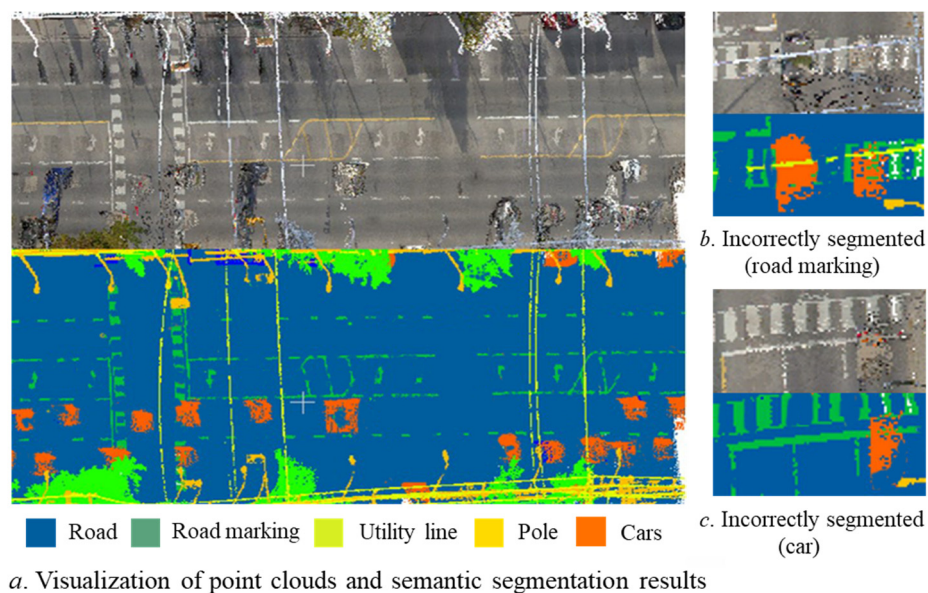

b. Incorrectly segmented (road marking)

c. Incorrectly segmented (car)

Road   **Road marking**   **Utility line**   **Pole**   **Cars**

a. Visualization of point clouds and semantic segmentation results

Figure 5. Comparison between colored point clouds and predicted segmentation results (Toronto-3D).

Table 1. Semantic segmentation (L002) results of Toronto-3D dataset %.

Method	mIoU (%)	OA (%)	IoU (%)							
			Road Surface	Road Mrk.	Natural.	Building	Util. Line	Pole	Car	Fence
Pointnet++	65.0	93.0	93.9	19.4	90.5	81.7	68.5	62.9	58.9	44.4
RandLA-Net	74.3	88.4	87.4	22.0	96.4	92.7	85.9	75.5	86.6	47.6
SCF-Net	71.5	93.5	91.4	19.6	90.9	87.3	78.5	72.6	84.6	47.4
Ours	73.9	95.3	95.7	25.9	94.0	86.3	81.5	71.8	78.1	58.1

As Table 1 indicates, our method outperforms the other methods in three of the eight categories; i.e., road surface, road marking, and fence. In particular, the IoU of the road surface in dense scans is higher than 95%. The proposed net is marginally inferior to RandLA-Net in terms of mIoU, but better in terms of OA. This is mainly owing to the suboptimal segmentation in the category of vertical objects (such as buildings, utility lines, and poles), which marginally reduces the mIoU. Figure 5 presents certain qualitative results at the intersection of L002. However, road markings could not be identified. These can be accurately extracted by the additional intensity and other information.

3.2.2. Evaluation on Semantic3D

In this work, we submit the results to the server and infer the dense scenes of the semantic-8 test set. The quantitative results are reported in Table 2. We consider an irregular road as an example because the ground truth of the test set is not publicly available. Its RGB colored point clouds and predicted segmentation results are presented in Figure 6, which shows the visualization results.

Table 2. Semantic segmentation (semantic-8) results of Semantic3D Dataset %.

Method	mIoU (%)	OA (%)	IoU (%)							
			Road Surface	Natural.	High Veg.	Low Veg.	Building	Infrastructure	Scanning Art.	Cars
Pointnet++	63.1	85.7	81.9	78.1	64.3	51.7	75.9	36.4	43.7	72.6
RandLA-Net	71.8	94.2	96	88.6	65.3	62.0	95.9	49.8	27.8	89.3
Ours	74.7	95.0	97.9	94.1	70.8	64.3	94.0	48.5	38.8	89.2

b. Incorrectly segmented (low vegetation)

c. Incorrectly segmented (infrastructure)

Road surface Natural terrain Low vegetation Infrastructure Cars and trucks

a. Visualization of point clouds and semantic segmentation results
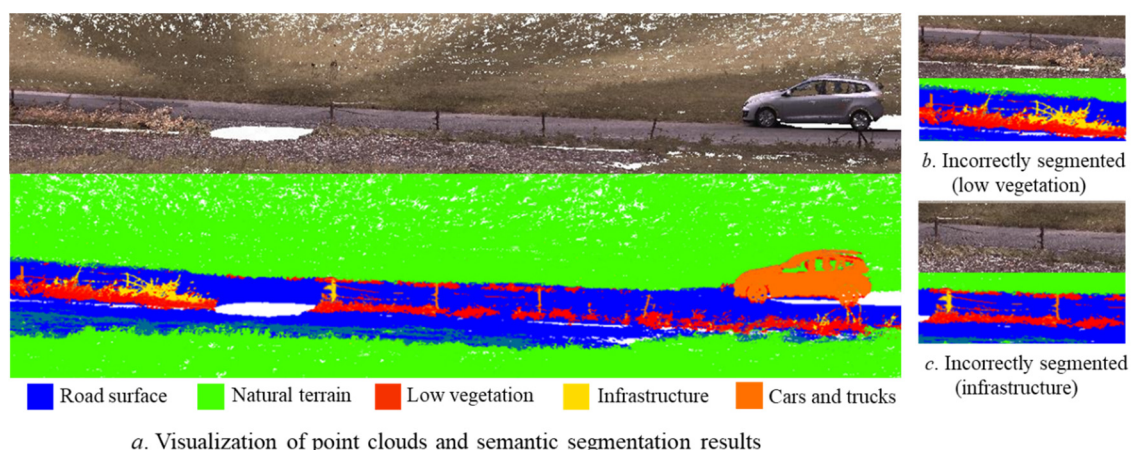
Figure 6. Comparison between colored point clouds and predicted segmentation results (Semantic3D).

As shown in this table, our method has the best mIoU and OA among all of the methods. Furthermore, the segmentation of the road surface exhibits better performance (an IoU of 97.9%) than the other categories. The categories of natural terrain, building, cars, and trucks have an IoU of over 89%. Figure 6 indicates that the low vegetation category, with low height and discrete distribution, is straightforwardly classified as infrastructure. Most errors

are caused by the low vegetation, infrastructure, and scanning artifact categories with few points and indistinct geometric structures, which renders the aggregated attentive pooling unit incapable of effectively obtaining the difference and similarity of its local features.

Meanwhile, we compared the improved SCF-Net with the SCF-Net based on the benchmark to validate the effectiveness of the improved SCF module. The results show that the proposed module could enrich the feature expression of input points' spatial information. Thereby, it achieves a higher application value for semantic segmentation. Overall, the improved net could be applied in the semantic segmentation of large-scale point clouds, particularly for road surfaces. This could ensure the accuracy and efficiency of road geometric information extraction in the subsequent steps.

3.3. Results of Road Geometric Information Extraction

Considering the road scenarios L002 in Toronto-3D and sg27_1 in Semantic3D as examples, the alpha-shape method is first applied to extract the road boundary when α is defined as 1 m (see Figure 7).

(**a**)   (**b**)
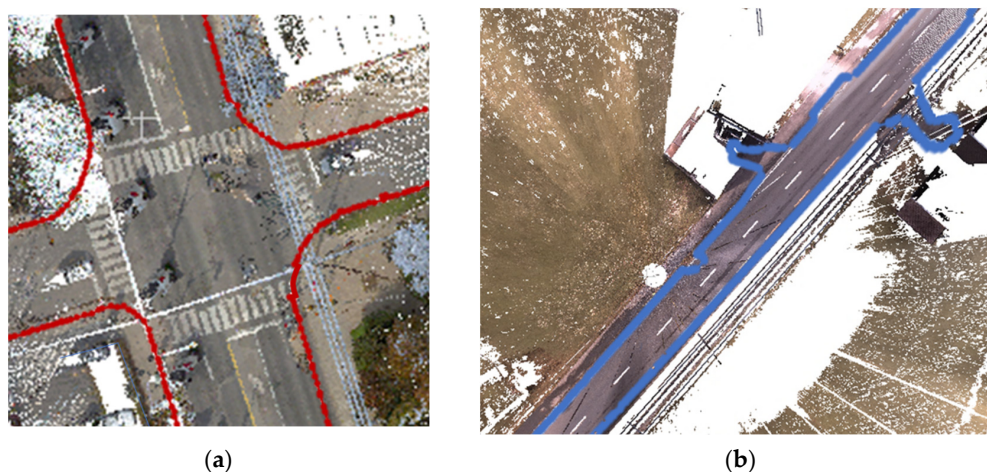
Figure 7. Extraction of the road boundary. (**a**) Intersection; (**b**) road.

To accurately obtain the elevation of the entire intersection, the DEM is constructed by the interpolation method based on the uniformly distributed point set. The generated point set and DEM are shown in Figures 8 and 9.
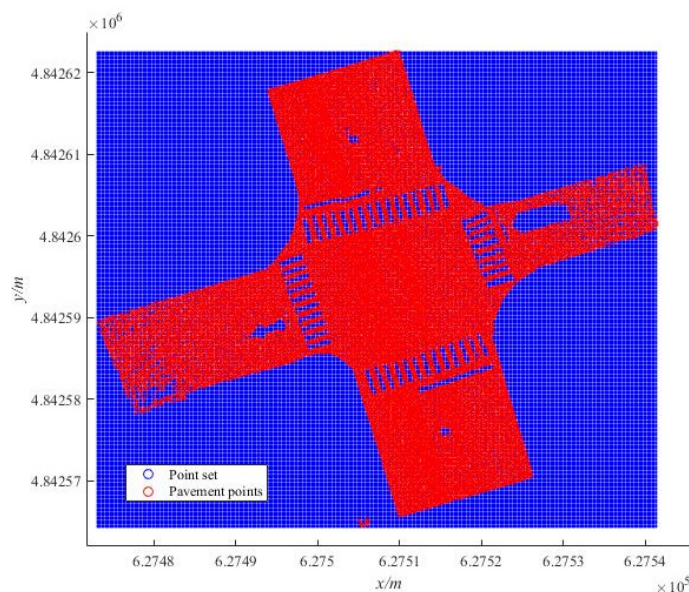

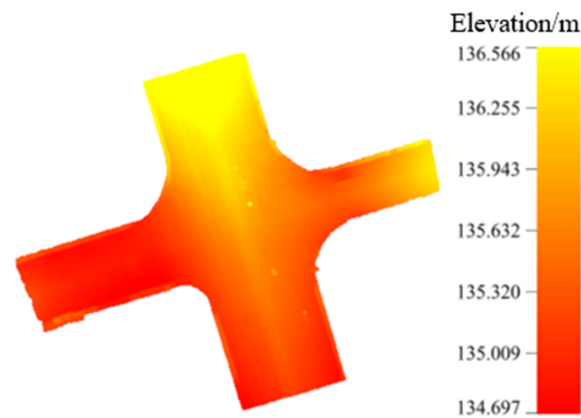**Figure 8.** Generated point set.

Figure 9. Generated DEM.

Thereafter, the Voronoi diagram method is used to obtain the centerline. To ensure the accuracy of extraction, the extraneous lines are removed based on the number of line segments (set as 25) in side branches through several iterations (see Figure 10). The original surface points are converted based on the centerline of the main road. The transformed boundary and centerline are presented in Figure 11. Meanwhile, the longitudinal slope is obtained from the elevation of the centerline expressed by Equation (8). As illustrated in Figure 12, the mean longitudinal slope of the road is −2.3%.
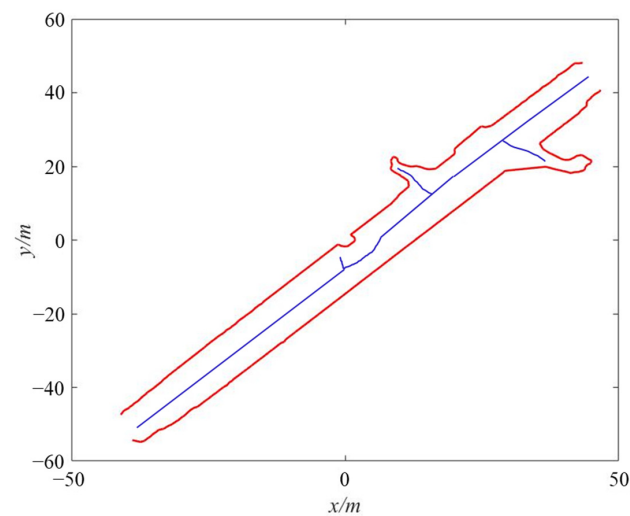
Figure 10. Generated original centerline.
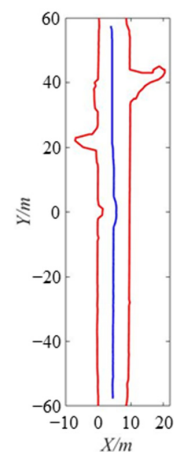
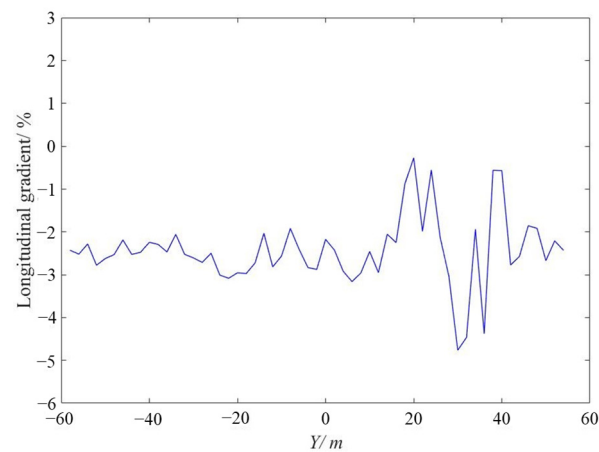**Figure 11.** Transformed boundary and centerline of the main road.

Figure 12. Longitudinal gradient.

In addition, the road width is calculated as the difference between the left and right sides (see Figure 13). As depicted in this figure, apparent road widening occurs at 20 m and 40 m because of the crossings. The cross-sectional profiles on both sides are fitted. The results are shown in Figure 14. As illustrated in this figure, the left and right cross slopes are 2.2 % and 2.3 % on average, respectively.
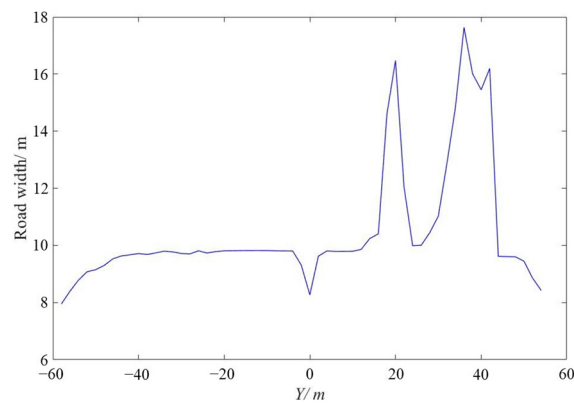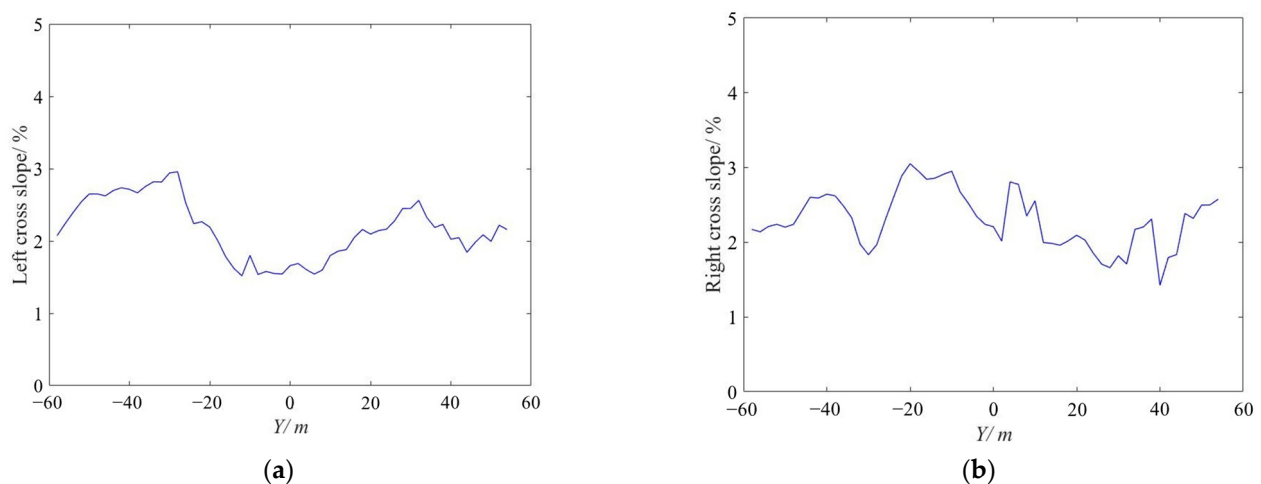

Figure 13. Road width.

Figure 14. Cross slopes of the road. (**a**) Left cross slope; (**b**) right cross slope.

To verify the reliability and accuracy of the geometric information extraction, manual measurement was employed in CloudCompare software to manually segment and measure

the slices of cross-sections every 2 m. Certain coordinate information can be displayed by visualization in CloudCompare software during the measurement process. The highest point of the cross-section (painted with the darkest red) is the midpoint of the road, owing to the form of the cross-section. For each cross-section, the left, right, and midpoint points could be selected to be exported in a batch and to calculate the left and right cross slopes (see Figure 15). The maximum and mean absolute errors of geometric information between the extracted methods and manual measurements are as shown in Table 3.
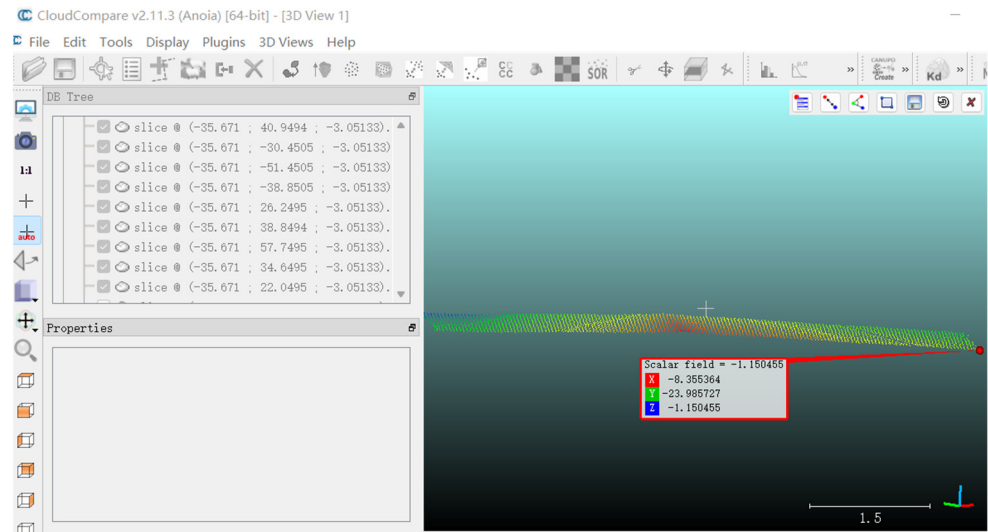

Figure 15. Manual measurement of the geometric information.

Table 3. Error Between Extraction Methods and Manual Measurement.

| Indicators | Geometric Information | | | |
| | Road Width/m | Longitudinal Gradient/% | Cross Slope | |
			Left Cross Slope/%	Right Cross Slope/%
Mean absolute error	0.0094	0.0091	0.0074	0.0073
Maximum absolute error	0.0530	0.0475	0.0238	0.0237
Location of Maximum absolute error/m	36	30	20	20

Table 3 demonstrates that the mean absolute error of road width between the extracted methods and manual measurements is less than 0.0094 m. Furthermore, the mean absolute errors for the other geometric information are less than 0.0091%. These indicate that the extracted methods are accurate and effective. The maximum and mean absolute errors for road width are larger than those for longitudinal gradient and cross slope. Based on the location of the maximum absolute error, we analyze the errors of geometric information from 20 to 40 m on the *Y*-coordinate to further investigate the cause of the larger errors. The comparison between the extracted and manually measured geometric information is presented in Table 4.

As shown in Table 4, the errors for different geometric information are larger when the *Y*-coordinates are 20 m and 30–36 m. Combined with the horizontal alignment, it can be observed that intersections exist in this range. This affects the surface segmentation. This directly results in the larger error of the road width, and further reduces the extraction accuracy of the geometric information.

3.4. Digital Modeling in BIM Environment

The 3D road scenario of sg27_1 is established using the proposed digital modeling process in Section 2.5. The road scenario consists of the road entity model, infrastructure

components, and other detailed designs. Among these, the process of establishing the road entity model should be given attention because of the road geometric information. More specifically, the road route is first interpolated to generate a series of interpolation points. Thereafter, these points are assessed and grouped to place the designed adaptive components. This establishes a road entity model. In this case study, the road alignment is straight, and the road width is approximately 10 m. Hence, 5% of the width is considered as the threshold value. Two interpolation points are grouped as the origin and destination of the adaptive road component. Subsequently, the placements of different infrastructures are determined based on boundary curves. The infrastructure components are manually placed and generated through Revit software. The surrounding vegetation and other elements are manually constructed based on the imported point clouds. The road entity is applied in the material of bituminous concrete. The established digital road scenario is compared with the LiDAR data (see Figure 16).

Table 4. Comparison between extracted and manually measured geometric information.

Location/m	Road Width/m			Longitudinal Gradient/%		
	Extracted Methods	Manual Measurement	Absolute Error	Extracted Methods	Manual Measurement	Absolute Error
20	16.4723	16.4228	0.0495	−0.2728	−0.2700	0.0028
22	12.0468	12.0348	0.0121	−1.9862	−1.9663	0.0199
24	9.9901	9.9931	0.0030	−0.5564	−0.5553	0.0011
26	10.0043	9.9944	0.0100	−2.1261	−2.1304	0.0043
28	10.4480	10.4376	0.0104	−3.0431	−3.0431	0.0000
30	11.0251	11.0140	0.0110	−4.7629	−4.8104	0.0475
32	12.8570	12.8312	0.0257	−4.4626	−4.5072	0.0446
34	14.8429	14.8132	0.0297	−1.9402	−1.9594	0.0192
36	17.6331	17.5801	0.0530	−4.3765	−4.4198	0.0433
38	16.0092	15.9611	0.0481	−0.5631	−0.5687	0.0056
40	15.4505	15.4195	0.0310	−0.5698	−0.5641	0.0057

Location/m	Left cross slope/%			Right cross slope/%		
	Extracted methods	Manual measurement	Absolute error	Extracted methods	Manual measurement	Absolute error
20	2.0960	2.1198	0.0238	2.0904	2.1141	0.0237
22	2.1436	2.1661	0.0225	2.0253	2.0465	0.0212
24	2.1628	2.1582	0.0046	1.8497	1.8457	0.0040
26	2.2789	2.2755	0.0034	1.7042	1.7017	0.0025
28	2.4485	2.4497	0.0012	1.6568	1.6577	0.0009
30	2.4504	2.4271	0.0233	1.8162	1.7989	0.0173
32	2.5608	2.5377	0.0231	1.7056	1.6902	0.0154
34	2.3259	2.3047	0.0212	2.1679	2.1482	0.0197
36	2.1869	2.1680	0.0189	2.2000	2.1810	0.0190
38	2.2301	2.2108	0.0193	2.3062	2.2863	0.0199
40	2.0245	2.0465	0.0220	1.4223	1.4378	0.0155

(a) The road scenario with point clouds in Revit

(b) 3D rendering of the road scenario in Revit

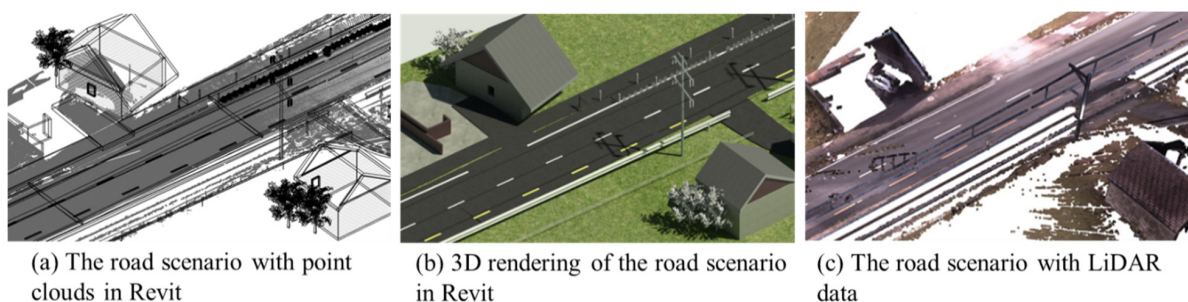(c) The road scenario with LiDAR data

Figure 16. Comparison of LiDAR data and the digital road scenario.

As shown in Figure 16, the road entity and infrastructure essentially achieve correspondences in the digital road scenarios. However, there are differences in the vegetation models because of the missing point clouds and different modeling approaches. Specifically, the morphology of low vegetation is incomplete owing to the occlusion of other objects and the larger distance from the sensor during point cloud collection. Although the surrounding vegetation can be effectively divided by the semantic segmentation network, these fail to be completely modeled with regard to the shapes and poses. Meanwhile, the vegetation is in the block distribution with denser locations. This cannot be sequentially realized by the modeling. Therefore, there is scope for improvement through multi-view images and the spatial geometry information of point clouds. It is likely to be feasible to accurately and completely model the surrounding vegetation.

4. Discussion

The results in Section 3 demonstrate the proposed framework can achieve the objective and make contributions, as shown in Section 1. First, the improved SCF-Net segments different categories of objects in road scenarios that can easily extract the geometric information and establish semantic-rich digital models. The quantitative results and visualizations show the improved SCF-Net is beneficial to enhance the segmentation performance in large-scale point cloud benchmarks. However, it can be argued that road markings, low vegetation, and infrastructure categories could not be identified because of missing points and indistinct geometric structures. Hence, a future direction for this research will be motivated by extracting more features and structures from point clouds or multiple data sources, such as optical images, GIS databases, and vehicle trajectory.

Second, a series of methods that extract the geometric information from point clouds of the segmented road surface is proposed. The mean absolute errors between the extracted and manually measured geometric information verify the reliability and accuracy of the extraction methods. Furthermore, Dynamo and Revit software are expected to generate digital models of the road entities and infrastructures based on the obtained semantic and geometric information. The nodes in Dynamo are used to import the data and establish the model. Nevertheless, the process of digital modeling is semi-automated. Manual modeling is required based on the imported point clouds for surrounding vegetation and other elements. Therefore, full automation is a future objective for digital modeling from LiDAR data of road scenarios.

5. Conclusions

In this study, an improved semantic segmentation network was used to divide the road surface and other infrastructures. The alpha-shape and Voronoi diagram methods were applied to extract the road boundary and centerline, and thereby obtain road geometric information. Subsequently, the road entity model and infrastructure components were constructed through Dynamo and Revit software. Finally, a digital road scenario was developed. The following conclusions could be drawn:

(1) The improved networks were validated by experiments on the large-scale point cloud benchmarks Toronto-3D and Semantic3D. The results of semantic segmentation showed that the OA of our net on the two datasets were 95.3 and 95.0%, respectively. Meanwhile, road surface achieved a better performance (IoU of 95.7 and 97.9%) than the other categories. This demonstrated that the proposed net is accurate and effective.

(2) Compared with the extracted and manually measured geometric information in CloudCompare software, the mean absolute error for road width was less than 0.0094 m, and those for the other geometric information were less than 0.0091%. Therefore, the extraction methods were effective for calculating the geometric information.

(3) The road entity and infrastructure modeling in BIM was established based on Dynamo and Revit software. This achieved correspondence in the digital road scenarios and LiDAR data.

This proposed framework is expected to provide transportation agencies with a workflow for updating the semantic and geomatic information of as-built roads and surrounding infrastructure as LiDAR technology and BIM technology become more common. It could also provide accurate descriptions for as-built road and infrastructure features, which extends beyond helping enhance the efficiency of inventorying to a potential reference in asset management and road safety inspection. Meanwhile, our study focused on the acquired data rather than the laser scanner system. It selected 3D coordinates and RGB information to represent the point clouds. This increased the applicability and portability of the proposed methods. In addition, the proposed methods could be combined with other data sources to accomplish road marking extraction and object recognition.

Finally, this study only demonstrated the applicability and accuracy of the proposed methods from the perspective of theoretical and manual measurements. Further field experiments are required to conduct geometric information extraction and validate its accuracy.

References

1. Jiang, F.; Ma, L.; Broyd, T.; Chen, W.; Luo, H. Building Digital Twins of Existing Highways Using Map Data Based on Engineering Expertise. *Autom. Constr.* **2022**, *134*, 104081. [CrossRef]
2. Jalayer, M.; Gong, J.; Zhou, H.; Grinter, M. Evaluation of Remote Sensing Technologies for Collecting Roadside Feature Data to Support Highway Safety Manual Implementation. *J. Transp. Saf. Secur.* **2015**, *7*, 345–357. [CrossRef]
3. Vaiana, R.; Perri, G.; Iuele, T.; Gallelli, V. A Comprehensive Approach Combining Regulatory Procedures and Accident Data Analysis for Road Safety Management Based on the European Directive 2019/1936/Ec. *Safety* **2021**, *7*, 6. [CrossRef]
4. Hou, Q.; Ai, C. A Network-Level Sidewalk Inventory Method Using Mobile LiDAR and Deep Learning. *Transp. Res. Part C Emerg. Technol.* **2020**, *119*, 102772. [CrossRef]
5. Holgado-Barco, A.; González-Aguilera, D.; Arias-Sanchez, P.; Martinez-Sanchez, J. Semiautomatic Extraction of Road Horizontal Alignment from a Mobile LiDAR System. *Comput.-Aided Civ. Infrastruct. Eng.* **2015**, *30*, 217–228. [CrossRef]
6. Gu, H.; Han, Y.; Yang, Y.; Li, H.; Liu, Z.; Soergel, U.; Blaschke, T.; Cui, S. An Efficient Parallel Multi-Scale Segmentation Method for Remote Sensing Imagery. *Remote Sens.* **2018**, *10*, 590. [CrossRef]
7. Holgado-Barco, A.; Riveiro, B.; González-Aguilera, D.; Arias, P. Automatic Inventory of Road Cross-Sections from Mobile Laser Scanning System. *Comput.-Aided Civ. Infrastruct. Eng.* **2017**, *32*, 3–17. [CrossRef]
8. Qiu, S.; Anwar, S.; Barnes, N. Semantic Segmentation for Real Point Cloud Scenes via Bilateral Augmentation and Adaptive Fusion. In Proceedings of the IEEE Computer Society Conference on Computer Vision and Pattern Recognition, Nashville, TN, USA, 20–25 June 2021; pp. 1757–1767.
9. Lin, Y.; Vosselman, G.; Cao, Y.; Yang, M.Y. Active and Incremental Learning for Semantic ALS Point Cloud Segmentation. *ISPRS J. Photogramm. Remote Sens.* **2020**, *169*, 73–92. [CrossRef]
10. Pierdicca, R.; Paolanti, M.; Matrone, F.; Martini, M.; Morbidoni, C.; Malinverni, E.S.; Frontoni, E.; Lingua, A.M. Point Cloud Semantic Segmentation Using a Deep Learning Framework for Cultural Heritage. *Remote Sens.* **2020**, *12*, 1005. [CrossRef]
11. Han, X.; Dong, Z.; Yang, B. A Point-Based Deep Learning Network for Semantic Segmentation of MLS Point Clouds. *ISPRS ISPRS J. Photogramm. Remote Sens.* **2021**, *175*, 199–214. [CrossRef]
12. Rodríguez-Cuenca, B.; García-Cortés, S.; Ordóñez, C.; Alonso, M.C. An Approach to Detect and Delineate Street Curbs from MLS 3D Point Cloud Data. *Autom. Constr.* **2015**, *51*, 103–112. [CrossRef]
13. Ibrahim, S.; Lichti, D. Curb-Based Street Floor Extraction From Mobile Terrestrial Lidar Point Cloud. *ISPRS-Int. Arch. Photogramm. Remote Sens. Spat. Inf. Sci.* **2012**, *XXXIX-B5*, 193–198. [CrossRef]

14. Xu, S.; Wang, R.; Zheng, H. Road Curb Extraction from Mobile LiDAR Point Clouds. *IEEE Trans. Geosci. Remote Sens.* **2017**, *55*, 996–1009. [CrossRef]

15. Kumar, P.; McElhinney, C.P.; Lewis, P.; McCarthy, T. An Automated Algorithm for Extracting Road Edges from Terrestrial Mobile LiDAR Data. *ISPRS J. Photogramm. Remote Sens.* **2013**, *85*, 44–55. [CrossRef]

16. Kumar, P.; Lewis, P.; McCarthy, T. The Potential of Active Contour Models in Extracting Road Edges from Mobile Laser Scanning Data. *Infrastructures* **2017**, *2*, 9. [CrossRef]

17. Guo, J.; Tsai, M.J.; Han, J.Y. Automatic Reconstruction of Road Surface Features by Using Terrestrial Mobile Lidar. *Autom. Constr.* **2015**, *58*, 165–175. [CrossRef]

18. Yadav, M.; Singh, A.K.; Lohani, B. Extraction of Road Surface from Mobile LiDAR Data of Complex Road Environment. *Int. J. Remote Sens.* **2017**, *38*, 4645–4672. [CrossRef]

19. Guo, Y.; Wang, H.; Hu, Q.; Liu, H.; Liu, L.; Bennamoun, M. Deep Learning for 3D Point Clouds: A Survey. *IEEE Trans. Pattern. Anal. Mach. Intell.* **2021**, *43*, 4338–4364. [CrossRef]

20. Lawin, F.J.; Danelljan, M.; Tosteberg, P.; Bhat, G.; Khan, F.S.; Felsberg, M. Deep Projective 3D Semantic Segmentation. *Lect. Notes Comput. Sci.* **2017**, *10424 LNCS*, 95–107.

21. Tchapmi, L.; Choy, C.; Armeni, I.; Gwak, J.; Savarese, S. SEGCloud: Semantic Segmentation of 3D Point Clouds. In Proceedings of the 2017 International Conference on 3D Vision, (3DV), Qingdao, China, 10–12 October 2017; pp. 537–547.

22. Graham, B.; Engelcke, M.; Van Der Maaten, L. 3D Semantic Segmentation with Submanifold Sparse Convolutional Networks. In Proceedings of the IEEE Computer Society Conference on Computer Vision and Pattern Recognition, Salt Lake City, UT, USA, 18–23 June 2018; pp. 9224–9232.

23. Meng, H.Y.; Gao, L.; Lai, Y.K.; Manocha, D. VV-Net: Voxel VAE Net with Group Convolutions for Point Cloud Segmentation. In Proceedings of the IEEE International Conference on Computer Vision 2019, Seoul, Republic of Korea, 27 October–2 November 2019; pp. 8499–8507.

24. Sha, A.; Yun, D.; Hu, L.; Tang, C. Influence of Sampling Interval and Evaluation Area on the Three-Dimensional Pavement Parameters. *Road Mater. Pavement Des.* **2021**, *22*, 1964–1985. [CrossRef]

25. Jing, H.; You, S. Point Cloud Labeling Using 3D Convolutional Neural Network. In Proceedings of the International Conference on Pattern Recognition, Cancun, Mexico, 4–8 December 2016; pp. 2670–2675.

26. Hu, Q.; Yang, B.; Xie, L.; Rosa, S.; Guo, Y.; Wang, Z.; Trigoni, N.; Markham, A. Learning Semantic Segmentation of Large-Scale Point Clouds With Random Sampling. *IEEE Trans. Pattern Anal. Mach. Intell.* **2021**, *44*, 1. [CrossRef]

27. Fan, S.Q.; Dong, Q.L.; Zhu, F.H.; Lv, Y.S.; Ye, P.J.; Wang, F.Y.; Ieee Comp, S.O.C. SCF-Net: Learning Spatial Contextual Features for Large-Scale Point Cloud Segmentation. In Proceedings of the IEEE/CVF Conference on Computer Vision and Pattern Recognition (CVPR), Nashville, TN, USA, 20–25 June 2021; pp. 14499–14508.

28. Yang, X.; Tang, L.; Niu, L.; Zhang, X.; Li, Q. Generating Lane-Based Intersection Maps from Crowdsourcing Big Trace Data. *Transp. Res. Part C Emerg. Technol.* **2018**, *89*, 168–187. [CrossRef]

29. Zhang, Z.; Li, J.; Guo, Y.; Yang, C.; Wang, C. 3D Highway Curve Reconstruction from Mobile Laser Scanning Point Clouds. *IEEE Trans. Intell. Transp. Syst.* **2020**, *21*, 4762–4772. [CrossRef]

30. Strygulec, S.; Muller, D.; Meuter, M.; Nunn, C.; Ghosh, S.; Wohler, C. Road Boundary Detection and Tracking Using Monochrome Camera Images. In Proceedings of the 16th International Conference on Information Fusion, (FUSION 2013), Istanbul, Turkey, 9–12 July 2013; pp. 864–870.

31. Mi, X.; Yang, B.; Dong, Z.; Chen, C.; Gu, J. Automated 3D Road Boundary Extraction and Vectorization Using MLS Point Clouds. *IEEE Trans. Intell. Transp. Syst.* **2022**, *23*, 5287–5297. [CrossRef]

32. Di Mascio, P.; Di Vito, M.; Loprencipe, G.; Ragnoli, A. Procedure to Determine the Geometry of Road Alignment Using GPS Data. *Procedia Soc. Behav. Sci.* **2012**, *53*, 1202–1215. [CrossRef]

33. Justo, A.; Soilán, M.; Sánchez-Rodríguez, A.; Riveiro, B. Scan-to-BIM for the Infrastructure Domain: Generation of IFC-Complaint Models of Road Infrastructure Assets and Semantics Using 3D Point Cloud Data. *Autom. Constr.* **2021**, *127*, 13. [CrossRef]

34. Soilán, M.; Justo, A.; Sánchez-Rodríguez, A.; Riveiro, B. 3D Point Cloud to BIM: Semi-Automated Framework to Define IFC Alignment Entities from MLS-Acquired LiDAR Data of Highway Roads. *Remote Sens.* **2020**, *12*, 2301. [CrossRef]

35. Tang, F.; Ma, T.; Zhang, J.; Guan, Y.; Chen, L. Integrating Three-Dimensional Road Design and Pavement Structure Analysis Based on BIM. *Autom. Constr.* **2020**, *113*, 17. [CrossRef]

36. Soilan, M.; Sanchez-Rodriguez, A.; del Rio-Barral, P.; Perez-Collazo, C.; Arias, P.; Riveiro, B. Review of Laser Scanning Technologies and Their Applications for Road and Railway Infrastructure Monitoring. *Infrastructures* **2019**, *4*, 58. [CrossRef]

37. Olsen, M.J.; Kuester, F.; Chang, B.J.; Hutchinson, T.C. Terrestrial Laser Scanning-Based Structural Damage Assessment. *J. Comput. Civ. Eng.* **2010**, *24*, 264–272. [CrossRef]

38. Kukko, A.; Kaartinen, H.; Hyyppa, J.; Chen, Y.W. Multiplatform Mobile Laser Scanning: Usability and Performance. *Sensors* **2012**, *12*, 11712–11733. [CrossRef]

39. Jaakkola, A.; Hyyppa, J.; Hyyppa, H.; Kukko, A. Retrieval Algorithms for Road Surface Modelling Using Laser-Based Mobile Mapping. *Sensors* **2008**, *8*, 5238–5249. [CrossRef] [PubMed]

40. Zhang, C.; Xu, S.; Jiang, T.; Liu, J.; Liu, Z.; Luo, A.; Ma, Y. Integrating Normal Vector Features into an Atrous Convolution Residual Network for Lidar Point Cloud Classification. *Remote Sens.* **2021**, *13*, 3427. [CrossRef]

41. Fang, L.; Shen, G.; You, Z.; Guo, Y.; Fu, H.; Zhao, Z.; Chen, C. A Joint Network of Point Cloud and Multiple Views for Roadside Objects Recognition from Mobile Laser Point Clouds. *Cehui Xuebao/Acta Geod. Cartogr. Sin.* **2021**, *50*, 1558–1573. [CrossRef]

42. AlHajri, M.F.; El-Hawary, M.E. Exploiting the Radial Distribution Structure in Developing a Fast and Flexible Radial Power Flow for Unbalanced Three-Phase Networks. *IEEE Trans. Power Deliv.* **2010**, *25*, 378–389. [CrossRef]

43. Guan, H.Y.; Li, J.; Yu, Y.T.; Chapman, M.; Wang, C. Automated Road Information Extraction From Mobile Laser Scanning Data. *IEEE Trans. Intell. Transp. Syst.* **2015**, *16*, 194–205. [CrossRef]

44. Ma, Y.; Easa, S.; Cheng, J.C.A.; Yu, B. Automatic Framework for Detecting Obstacles Restricting 3D Highway Sight Distance Using Mobile Laser Scanning Data. *J. Comput. Civ. Eng.* **2021**, *35*, 19. [CrossRef]

45. Al-Tamimi, M.S.H.; Sulong, G.; Shuaib, I.L. Alpha Shape Theory for 3D Visualization and Volumetric Measurement of Brain Tumor Progression Using Magnetic Resonance Images. *Magn. Reson. Imaging* **2015**, *33*, 787–803. [CrossRef]

46. Widyaningrum, E.; Peters, R.Y.; Lindenbergh, R.C. Building Outline Extraction from ALS Point Clouds Using Medial Axis Transform Descriptors. *Pattern Recognit.* **2020**, *106*, 15. [CrossRef]

47. Tejenaki, S.A.K.; Ebadi, H.; Mohammadzadeh, A. A New Hierarchical Method for Automatic Road Centerline Extraction in Urban Areas Using LIDAR Data. *Adv. Space Res.* **2019**, *64*, 1792–1806. [CrossRef]

48. Younas, S.; Figley, C.R. Development, Implementation and Validation of an Automatic Centerline Extraction Algorithm for Complex 3D Objects. *J. Med. Biol. Eng.* **2019**, *39*, 184–204. [CrossRef]

49. Tan, W.K.; Qin, N.N.; Ma, L.F.; Li, Y.; Du, J.; Cai, G.R.; Yang, K.; Li, J.; Ieee Comp, S.O.C. Toronto-3D: A Large-Scale Mobile LiDAR Dataset for Semantic Segmentation of Urban Roadways. In Proceedings of the IEEE/CVF Conference on Computer Vision and Pattern Recognition (CVPR), Seattle, WA, USA, 13–19 June 2020; pp. 797–806.

50. Hackel, T.; Wegner, J.D.; Savinov, N.; Ladicky, L.; Schindler, K.; Pollefeys, M. Large-Scale Supervised Learning For 3D Point Cloud Labeling: Semantic3d.Net. *Photogramm. Eng. Remote Sens.* **2018**, *84*, 297–308. [CrossRef]